Supplemental Information

Beyond Lithium Lanthanum Titanate: Metal-Stable Hafnium Perovskite Electrolytes for Solid-State Batteries

Ahmed H. Biby,[1] Basant A. Ali,[2] and Charles B. Musgrave* [2,3,4]
[1]Materials Science and Engineering Program, University of Colorado Boulder, Boulder, CO 80309, USA
[2]Department of Chemical and Biological Engineering, University of Colorado, Boulder, Colorado 80303, USA
[3]Department of Chemical Engineering, University of Utah, Salt Lake City, Utah, 84112, USA
[4]Department of Materials Science and Engineering, University of Utah, Salt Lake City, Utah, 84112, USA
*Correspondence should be addressed to charles.musgrave@utah.edu

Structural models

According to Chambers et. al., the tetragonal I4/mcm LLTO is the ground-state polymorph.[1] Thus, we retrieved the tetragonal I4/mcm $SrTiO_3$ (mp-4651) from the materials project (MP) repository as a reference pristine perovskite structure.[2] We chose $SrTiO_3$ because its A-site ionic radius (Sr^{2+}) is close to the ionic radius of La^{3+}.[3] At different stages of the study, two distinct working-ion concentration regimes were analyzed: a computationally efficient low concentration (lc) $A'_{0.125}A''_{0.625}\square_{0.25}B_1X_3$ ($A'_1A''_5\square_2B_8X_{24}$) for compositional screening with 38-atom unit cell and a high concentration (hc) $A'_{0.3125}A''_{0.5625}\square_{0.125}B_1X_3$ ($A'_5A''_9\square_2B_{16}X_{48}$) for the in-depth study stage with 78-atom unit cell. A’, A”, □, B, and X are the working-ion, large-ionic-radius cation, A-site vacancy, small-ionic-radius cation, and anion, respectively.

To obtain the desired lc and hc compositions, we implemented the `SupercellTransformation`, `RemoveSitesTransformation`, and `SubstitutionTransformation` of the transformations.standard_transformations module from Pymatgen.[4] Further, we used the `DLSVolumePredictor` module from Pymatgen to obtain better initial structures upon changing the composition of the reference pristine perovskite structure.

Structural stability

To evaluate the perovskite structural stability, we calculated the Goldschmidt tolerance factor (t), the octahedral factor (μ), and the machine-learned tolerance factor τ using Shannon ionic radii and the weighted average effective ionic radius for the A-site species ($\overline{r_A}$) for all the studied compositions, as described in **eqs. S1**, **S2**, **S3,** and **S4**, respectively. [3,5–8]

$$t = \frac{\overline{r_A} + r_X}{\sqrt{2}(r_B + r_X)} \qquad \text{(S1)}$$

$$\mu = \frac{r_B}{r_X} \qquad \text{(S2)}$$

$$\tau = \frac{r_X}{r_B} - n_A\left(n_A - \frac{\overline{r_A}/\, r_B}{ln(\overline{r_A}/\, r_B\,)}\right) \quad \text{(S3)}$$

$$\overline{r_A} = \sum_{i=1}^{n} x_i \,.\, r_{A_i} \quad \text{(S4)}$$

Where r_B, r_X, n_A, n, x_i, and r_{A_i} are the B-site species ionic radius, the X-site species ionic radius, the weighted average of the oxidation state of A (i.e, 2+ for this study), the number of species co-occupying the A-site, the ratio of the A_i at the A-sites, and the effective ionic radius of a 12-coordinated cation A_i, respectively. Shannon ionic radii were used,[3] while the radius of the vacancy was assumed to be equal to Sr^{2+}'s ionic radius of the reference pristine perovskite. The stable structures should satisfy $0.75 < t < 1$, $\mu > 0.414$, and $\tau < 4.18$. The t, μ, and τ values of the studied compositions are provided in **Table 1** and **Table S1.**

Table S1 Summary of compositional screening results for the hc compositions, including evaluations of structural, thermodynamic, and electrochemical stability, and electronic bandgaps. t is the Goldschmidt tolerance factor, μ the octahedral factor, τ machine-learned tolerance factor, E_f the formation energy, E_D the decomposition energy, E_W the electrochemical stability window relative to the working-ion, and E_g the electronic bandgap computed using the HSE DFT functional.

Structure	t	μ	τ	E_f (eV/atom)	E_D (eV/atom)	E_g (eV)	E_W (eV)	Comment
hc-NLTO	0.98	0.43	3.85	-3.41	-5.36	3.52	[0, 3.03]*	Same as lc-NLTO
hc-NLZrO	0.93	0.51	3.84	-3.62	-5.55	5.21	[0, 2.68]	Same as lc-NLZrO
hc-NLHfO	0.93	0.51	3.82	-3.71	-5.83	5.60	[0, 2.26]	Same as lc-NLHfO
hc-LLTO	0.96	0.43	3.89	-3.42	-5.37	3.82	[1.53, 3.45]	Same as lc-LLTO
hc-LLZrO	0.91	0.51	3.96	-3.62	-5.55	5.43	[0, 3.19]*	Same as lc-LLZrO
hc-LLHfO	0.92	0.51	3.93	-3.71	-5.78	5.55	[0, 3.28]*	Same as lc-LLHfO

** Denotes metastable electrochemical stability, indicating that the reduction potential onset is metastable.*

Computational Details

Throughout the study, spin-polarized density functional theory (DFT) calculations were performed using the Vienna Ab initio Simulation Package (VASP).[9] The projected augmented wave (PAW) method was employed to model interactions between valence electrons and core ions, with the exchange-correlation potential described using the Perdew–Burke–Ernzerhof (PBE) generalized gradient approximation (GGA) functional.[10] For energy minimization, a plane-wave basis set expansion with a cutoff energy of 520 eV was used, alongside electronic convergence and ionic force thresholds of 10^{-5} eV and 0.05 eV/Å, respectively. Γ-centered k-point meshes of 2×4×3 and 2×2×3 were used for low- and high-concentration cells, respectively. We used HSE06 hybrid functional to calculate the electronic bandgaps.[11]

Thermodynamic and electrochemical stability calculations

The configurational entropy (S) was calculated using **eq. S5** to obtain the entropic contribution (TS) to the free energy.[1] At 300 K, TS was found to be 5 meV/atom for lc and hc compositions, respectively.

$$S = \frac{-k_B \sum_{j=1}^{n} \sum_k p_{jk} \ln{(p_{jk})}}{n} \quad \text{(S5)}$$

where n and p_{jk} are the number of sites in a given structure, and p_{jk} is the partial occupancy of element k at site j.

We calculated the average ensemble energy $\langle E \rangle$ via the summation of the products of each configuration's energy (E_i) and its corresponding probability (P_i) across all the calculated configurations, under the assumption of a canonical ensemble at constant temperature and pressure, as shown in **eqs. S6** and **S7**,[1]

$$\langle E \rangle = \sum_i P_i E_i \quad \text{(S6)}$$

$$P_i = \frac{e^{-E_i/_{kT}}}{\sum_m e^{-E_m/_{kT}}} \quad \text{(S7)}$$

where T is temperature in Kelvin and k is Boltzmann's constant.

Notably, we calculated the difference between the average ensemble energy and the least-energy configurations (LECs) for several structures and found them to be within 5 meV. These findings confirm that LEC energy, without considering the entropic contribution, provides a reliable basis for further calculations.

To calculate the thermodynamic and electrochemical stabilities, phase diagrams were constructed using the `PhaseDiagram` module of Pymatgen.[4] The competing phases from the MP repository, and the DFT energies of the LECs from our calculations served as the data points for constructing the phase diagrams.[2]

To assess electrochemical stability, the stable electrochemical window is defined as the potential range over which a given phase exhibits decomposition energies ≥ -50 meV/atom, as described in **eq. S8**.[12] This metastability threshold was selected to account for the DFT margin of error that introduces errors into the calculated energies and for the metastability stemming from the kinetic-stabilization effects,[13]

$$\Delta E_D^{open}(phase\,,\, \mu_{wi}) = E_{eq}\left[C_{eq}(C, \mu_{wi})\right] - E(phase) - \Delta n_{wi}\mu_{wi} \qquad \text{(S8)}$$

where ΔE_D^{open} is the decomposition reaction energy at a given chemical potential (μ_{wi}) against the working-ion (wi), C_{eq} and E_{eq} are the composition and the total formation energy of the competing phase equilibria at a given chemical potential μ_{wi}, $E(phase)$ is the formation energy of the phase of interest, and Δn the change in the number atoms of a given element at chemical potential μ_{wi}.

In our thermodynamic and electrochemical calculations, we combined our DFT results for PTEs with thermodynamic data from the MP repository. The MP repository applies the MP2020 energy correction to standardize the energy scale by fitting energy corrections to experimental data, ensuring consistency across material entries within its database.[14] However, applying this correction strictly requires adherence to the MP conventions for VASP input parameters defined in the `pymatgen.io.vasp.sets.MPRelaxSet`. Using this compatibility scheme with calculations based on different parameters is not valid.[4] In this study, we employed more stringent VASP setup parameters than that adopted in the MP repository, necessitating a customized correction to avoid erroneous results upon combining our data with thermodynamic data from the MP repository. To address this, we fit our energy correction to the well-established reduction potential onset of LLTO (~1.7 V vs. Li/Li$^+$) to determine the appropriate correction, as shown in **Figure S1(a)**.[12,13] Additionally, to validate our correction, the calculated formation energy of LLTO (-3.5 eV/atom) closely matches values reported in the literature.[1]

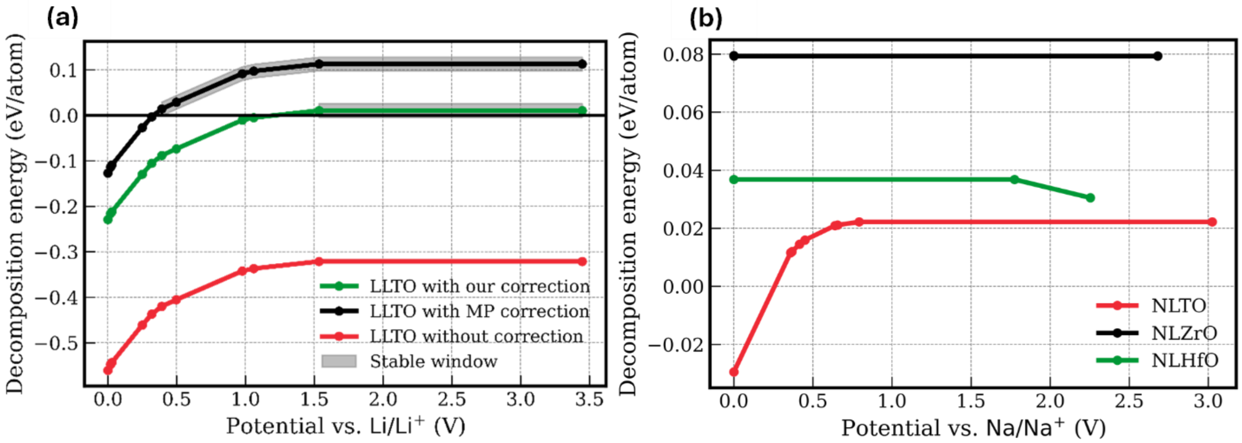

Figure S1 (a) LLTO Electrochemical windows using various corrections, where the MP correction applies the MP2020 energy correction to standardize energy scales by fitting to experimental data. While our correction was determined by fitting to the reduction potential onset of LLTO (~1.7 V vs. Li/Li$^+$). **(b)** Electrochemical stability of NLTO, NLZrO, and NLHfO, where NLZrO and NLHfO demonstrated stability against metal anodes with high oxidation potential onset.

Nudged Elastic Band Calculations

To evaluate the working-ion diffusion barriers for PTEs, we computed the minimum energy pathway (MEP) between a working-ion (A-site) to a neighboring vacant A-site. We used the climbing-image solid-state nudged elastic band (CI SS-NEB) method at the PBE DFT level of theory, where the diffusion path was divided into a number of equidistant configurations (images).[15–17] Fortunately, the LECs feature a neighboring vacant A-site adjacent to a working-ion. For a given PTE, the LEC itself was used as the initial image, while the final image was prepared by exchanging the working-ion with its adjacent vacant A-site. To ensure precise CI SS-NEB calculations, stricter DFT setup was applied, including an electronic energy convergence threshold of 10^{-6} eV and an ionic force threshold of 0.01 eV/Å for the geometry optimization of the initial and final images. To compute the MEP, a Γ-point centered 2×4×3 and 2×2×3 k-point mesh was used for Brillouin zone integration for the lc and hc compositions, respectively. A plane-wave basis set expansion with a cutoff energy of 520 eV was used. The relaxation of electronic degrees of freedom was terminated when the change in total energies between two consecutive electronic steps was < 10^{-6} eV. The structural relaxations were completed when the residual force on each atom was < 0.025 eV/Å. We report the 13-image MEP representing steps along the MEP from the initial state (A-site) moving toward the neighboring vacant A-site.

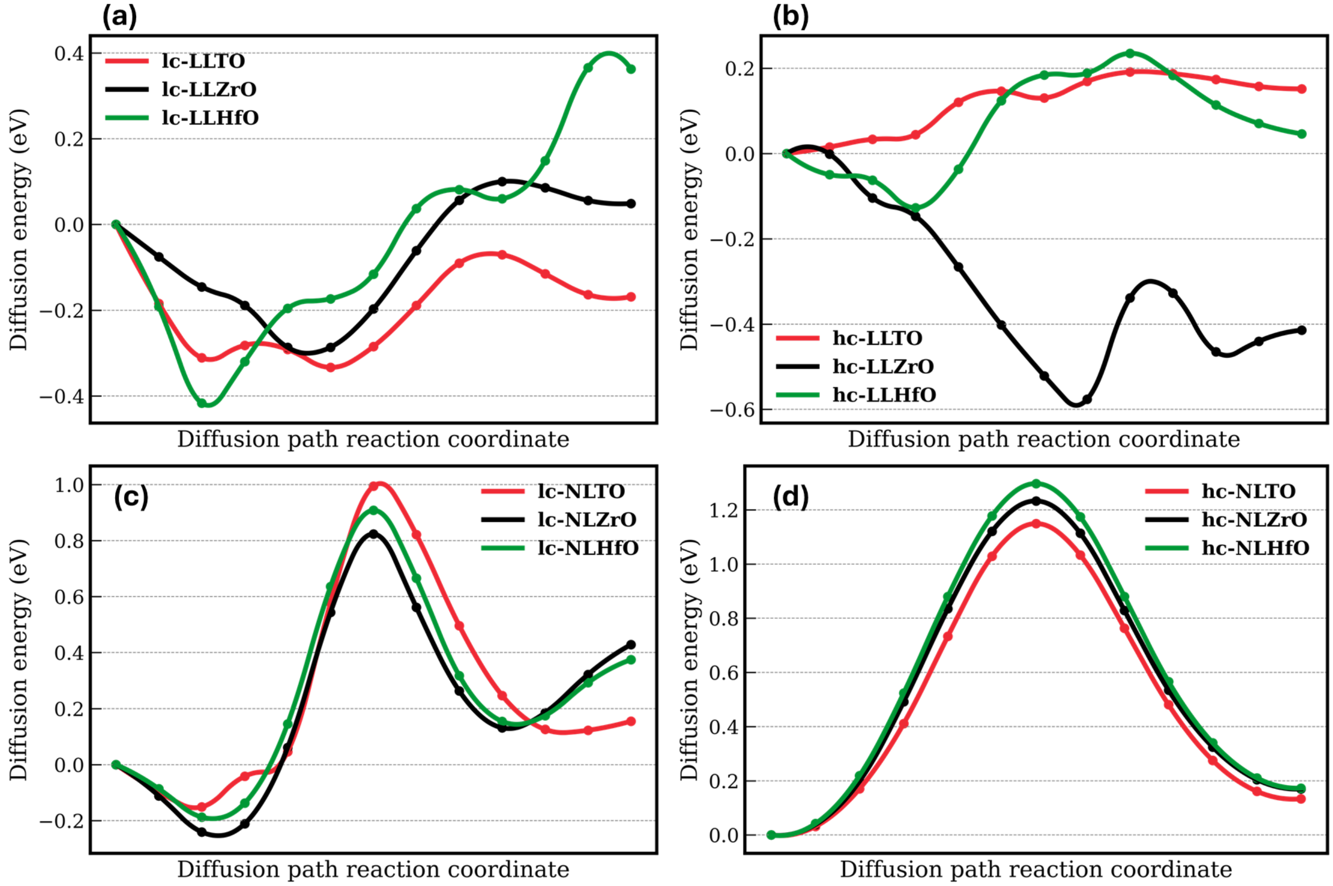

Figure S2 (a-d) CI-SS-NEB-computed approximate minimum energy pathway (MEP) for working-ion diffusion in various PTE compositions. The MEP starts from the initially working-ion occupied A-site, passes through the octahedral transport channel bottleneck (the transition state), and proceeds toward the initially vacant neighboring A-site.

Table S2 Diffusion barriers and bottlenecks for lc and hc compositions for LLTO, LLZrO, LLHfO, NLTO, NLZrO, and NLHfO. While LLZrO and LLHfO exhibit reasonable diffusion barriers, these values remain consistently higher than those of LLTO. On the other hand, the studied PTEs are deemed impractical for use in metal sodium all-solid-state batteries with diffusion barriers exceeding 0.85 eV.

Structure	Forward diffusion barrier (eV)	Backward diffusion barrier (eV)	Kinetic-resolved barrier (eV)	Bottleneck (Å)
lc-LLTO	0.263	0.311	0.287	0.722
lc-LLZrO	0.387	0.287	0.337	0.832
lc-LLHfO	0.498	0.417	0.458	0.823
lc-NLTO	1.145	0.871	1.008	0.817
lc-NLZrO	1.064	0.692	0.878	0.981
lc-NLHfO	1.095	0.753	0.924	0.969
hc-LLTO	0.146	0.040	0.093	1.226
hc-LLZrO	0.249	0.576	0.413	1.625
hc-LLHfO	0.362	0.188	0.275	0.949
hc-NLTO	1.149	1.016	1.083	1.078
hc-NLZrO	1.233	1.063	1.148	0.968
hc-NLHfO	1.297	1.124	1.211	0.951

Mechanical Properties

To ensure precision in mechanical property calculations, stricter criteria of 10^{-8} eV for electronic energy convergence and 0.01 eV/Å for ionic force convergence were applied for geometry optimizations. This study employed the stress-strain method with lattice strains of ±(0.005, 0.01, and 0.015) to evaluate the mechanical properties of triclinic cells, after undergoing geometry optimization from the initial tetragonal cells. Due to their low symmetry, triclinic cells have 21 independent elastic constants that can be calculated by applying finite distortions to the unit cell. For a triclinic cell to be mechanically stable, its elastic constants must satisfy the Born stability criteria.[18–20] The general stability criteria for the elastic constant matrix **C** are:

1. Positive definiteness, which must have all positive eigenvalues of **C**.
2. The leading principal minors of the matrix must be positive.
3. All elastic constants for diagonal terms are positive.

The bulk modulus (B) and shear modulus (G) of the polycrystalline state were calculated using the Voigt–Reuss–Hill (VRH) approximation,[21] and the Young's modulus (E) was approximated as follows:[22]

$E=9BG/(3B+G)$

Within the linear elastic region, the stress (σ) and strain (ϵ) satisfy the generalized Hooke's law, which can be expressed in the Voigt notation

$$\sigma_i = \sum_{j=1}^{6} C_{ij}\epsilon_j$$

where the strain or stress is represented as a vector with six independent components of $1 \leq i, j \leq 6$ and C_{ij} is the second-order elastic stiffness tensor shown by a 6 × 6 symmetric matrix in units of GPa.[23]

$$\boldsymbol{C} = \begin{bmatrix} C_{11} & C_{12} & C_{13} & C_{14} & C_{15} & C_{16} \\ C_{12} & C_{22} & C_{23} & C_{24} & C_{25} & C_{26} \\ C_{13} & C_{23} & C_{33} & C_{34} & C_{35} & C_{36} \\ C_{14} & C_{24} & C_{34} & C_{44} & C_{45} & C_{46} \\ C_{15} & C_{25} & C_{35} & C_{45} & C_{55} & C_{56} \\ C_{16} & C_{26} & C_{36} & C_{46} & C_{56} & C_{66} \end{bmatrix}$$

a. Mechanical criteria for SSE

A previous study computed the shear modulus for BCC Li metal as 4.25 GPa, implying that to inhibit dendrite formation solid-state electrolytes (SSEs) must have room temperature shear modulus values greater than ~8.5 GPa.[24,25] However, a decrease in the elastic modulus values have been reported for increased temperatures. Because the calculations are for the ground state (0 K), the shear moduli are high. However, it was reported that near 0 K, the elastic modulus could increase by 5%, meaning that to prevent dendrite formation shear moduli should be ~ 8.9 GPa.

The universal anisotropy number (UAN) quantifies the degree of anisotropy in a solid-state electrolyte (SSE).[26] A UAN greater than 1 indicates significant directional dependence of mechanical properties (anisotropic), suggesting that the SSE exhibits different stiffness, strength, or ductility in different crystallographic directions.[26] Understanding the UAN helps in optimizing materials for specific applications where uniform properties are desired

The Debye temperature in SSEs indicates the temperature range over which lattice vibrations (phonons) significantly contribute to thermal properties. A higher Debye temperature suggests stronger bonding interactions and higher stiffness, which can enhance ionic conductivity at elevated temperatures. It reflects the material's ability to withstand thermal stress, influencing the stability and performance of SSEs in battery applications.[27] Thus, the Debye temperature serves as a useful parameter for predicting thermal behavior and phase stability in solid-state electrolytes.

b. Stiffness Tensor C_{ij} (in GPa)

LEC-hc-LLTO

$$\begin{bmatrix} 422.840 & 204.799 & 214.909 & -6.354 & -0.884 & 8.239 \\ 204.799 & 415.417 & 229.904 & 0.569 & -8.400 & 10.135 \\ 214.909 & 229.904 & 360.401 & 7.081 & -2.241 & -7.543 \\ -6.354 & 0.569 & 7.081 & 95.915 & 5.269 & 3.018 \\ -0.884 & -8.400 & -2.241 & 5.269 & 97.555 & -1.748 \\ 8.239 & 10.135 & -7.543 & 3.018 & -1.748 & 89.535 \end{bmatrix}$$

LEC -hc-LLZrO (unstable)

$$\begin{bmatrix} 222.825 & 89.530 & 75.276 & -2.900 & -0.611 & 6.944 \\ 89.530 & 232.339 & 79.943 & -12.319 & -1.004 & 4.785 \\ 75.276 & 79.943 & 216.676 & -19.028 & -5.524 & 5.598 \\ -2.900 & -12.319 & -19.028 & 68.848 & 5.022 & -8.862 \\ -0.611 & -1.004 & -5.524 & 5.022 & -51.022 & -1.483 \\ 6.944 & 4.785 & 5.598 & -8.862 & -1.483 & 86.143 \end{bmatrix}$$

2nd LEC -hc-LLZrO

$$\begin{bmatrix} 206.815 & 99.309 & 73.793 & 15.727 & -9.890 & 7.680 \\ 99.309 & 204.569 & 76.624 & -2.716 & 1.055 & -21.473 \\ 73.793 & 76.624 & 129.561 & -1.364 & 6.214 & -3.488 \\ 15.727 & -2.716 & -1.364 & 59.471 & 1.253 & -17.273 \\ -9.890 & 1.055 & 6.214 & 1.253 & 64.515 & 12.609 \\ 7.680 & -21.473 & -3.488 & -17.273 & 12.609 & 71.524 \end{bmatrix}$$

LEC -hc-LLHfO

$$\begin{bmatrix} 246.018 & 102.786 & 74.642 & -1.633 & 1.370 & -10.226 \\ 102.786 & 234.038 & 79.833 & -7.900 & -3.392 & -0.500 \\ 74.642 & 79.833 & 228.702 & -4.709 & 0.610 & -6.610 \\ -1.633 & -7.900 & -4.709 & 66.243 & 2.599 & -1.570 \\ 1.370 & -3.392 & 0.610 & 2.599 & 66.354 & 4.272 \\ -10.226 & -0.500 & -6.610 & -1.570 & 4.272 & 83.522 \end{bmatrix}$$

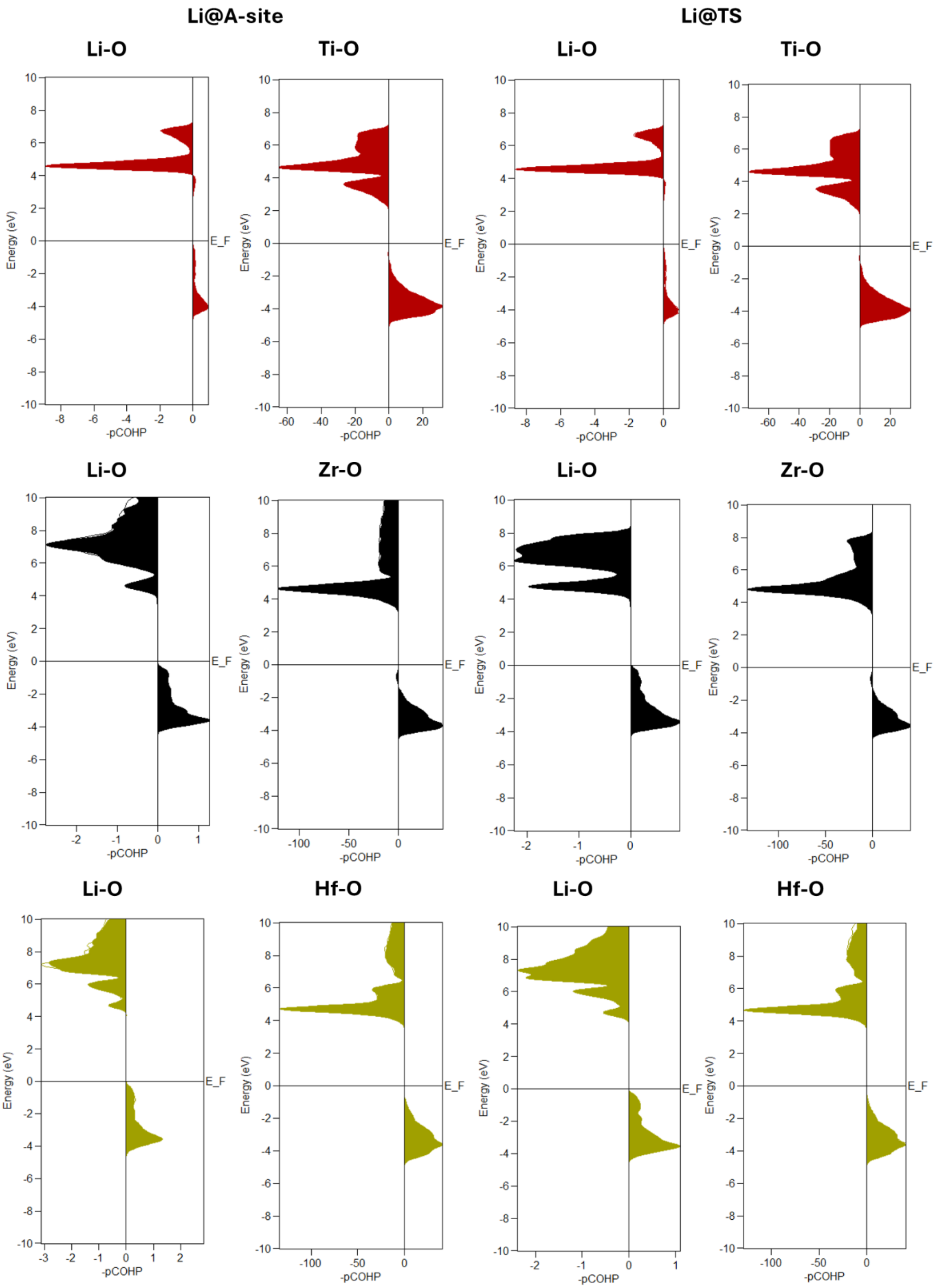

Figure S3 pCOHP analysis for LLTO (red), LLZrO (Black), and LLHfO (Olive green). The analysis was conducted for the initial (Li@A-site) and TS (Li@TS) configurations obtained from the NEB images.

References

(1) Chambers, M. S.; Chen, J.; Sacci, R. L.; McAuliffe, R. D.; Sun, W.; Veith, G. M. Memory Effect on the Synthesis of Perovskite-Type Li-Ion Conductor $Li_xLa_{2/3-x/3}TiO_3$ (LLTO). *Chem. Mater.* **2024**, *36* (3), 1197–1213. https://doi.org/10.1021/acs.chemmater.3c01928.

(2) Jain, A.; Ong, S. P.; Hautier, G.; Chen, W.; Richards, W. D.; Dacek, S.; Cholia, S.; Gunter, D.; Skinner, D.; Ceder, G.; Persson, K. A. Commentary: The Materials Project: A Materials Genome Approach to Accelerating Materials Innovation. *APL Materials* **2013**, *1* (1), 011002. https://doi.org/10.1063/1.4812323.

(3) Shannon, R. D. Revised Effective Ionic Radii and Systematic Studies of Interatomic Distances in Halides and Chalcogenides. *Acta Crystallographica Section A* **1976**, *32* (5), 751–767. https://doi.org/10.1107/S0567739476001551.

(4) Ong, S. P.; Richards, W. D.; Jain, A.; Hautier, G.; Kocher, M.; Cholia, S.; Gunter, D.; Chevrier, V. L.; Persson, K. A.; Ceder, G. Python Materials Genomics (Pymatgen): A Robust, Open-Source Python Library for Materials Analysis. *Computational Materials Science* **2013**, *68*, 314–319. https://doi.org/10.1016/j.commatsci.2012.10.028.

(5) Goldschmidt, V. M. Die Gesetze der Krystallochemie. *Naturwissenschaften* **1926**, *14* (21), 477–485. https://doi.org/10.1007/BF01507527.

(6) Li, C.; Soh, K. C. K.; Wu, P. Formability of ABO_3 Perovskites. *Journal of Alloys and Compounds* **2004**, *372* (1), 40–48. https://doi.org/10.1016/j.jallcom.2003.10.017.

(7) Ji, D. H.; Wang, S. L.; Ge, X. Z.; Zhang, Q. Q.; Zhang, C. M.; Zeng, Z. W.; Bai, Y. The Maximum Predicted Content of Cation Vacancies in Inorganic and Organic–Inorganic Perovskites: The Role of the Tolerance Factor. *Phys. Chem. Chem. Phys.* **2017**, *19* (26), 17121–17127. https://doi.org/10.1039/C7CP01792H.

(8) Bartel, C. J.; Sutton, C.; Goldsmith, B. R.; Ouyang, R.; Musgrave, C. B.; Ghiringhelli, L. M.; Scheffler, M. New Tolerance Factor to Predict the Stability of Perovskite Oxides and Halides. *Sci. Adv.* **2019**, *5* (2), eaav0693. https://doi.org/10.1126/sciadv.aav0693.

(9) Kresse, G.; Furthmüller, J. Efficient Iterative Schemes for *Ab Initio* Total-Energy Calculations Using a Plane-Wave Basis Set. *Physical Review B* **1996**, *54* (16), 11169. https://doi.org/10.1103/PhysRevB.54.11169.

(10) Perdew, J. P.; Burke, K.; Ernzerhof, M. Generalized Gradient Approximation Made Simple. *Physical Review Letters* **1996**, *77* (18), 3865–3868. https://doi.org/10.1103/PhysRevLett.77.3865.

(11) Heyd, J.; Scuseria, G. E.; Ernzerhof, M. Hybrid Functionals Based on a Screened Coulomb Potential. *The Journal of Chemical Physics* **2003**, *124* (21), 219906. https://doi.org/10.1063/1.1564060.

(12) Zhu, Y.; He, X.; Mo, Y. First Principles Study on Electrochemical and Chemical Stability of Solid Electrolyte–Electrode Interfaces in All-Solid-State Li-Ion Batteries. *J. Mater. Chem. A* **2016**, *4* (9), 3253–3266. https://doi.org/10.1039/C5TA08574H.

(13) Schwietert, T. K.; Vasileiadis, A.; Wagemaker, M. First-Principles Prediction of the Electrochemical Stability and Reaction Mechanisms of Solid-State Electrolytes. *JACS Au* **2021**, *1* (9), 1488–1496. https://doi.org/10.1021/jacsau.1c00228.

(14) Wang, A.; Kingsbury, R.; McDermott, M.; Horton, M.; Jain, A.; Ong, S. P.; Dwaraknath, S.; Persson, K. A. A Framework for Quantifying Uncertainty in DFT Energy Corrections. *Sci Rep* **2021**, *11* (1), 15496. https://doi.org/10.1038/s41598-021-94550-5.

(15) Henkelman, G.; Uberuaga, B. P.; Jónsson, H. A Climbing Image Nudged Elastic Band Method for Finding Saddle Points and Minimum Energy Paths. *The Journal of Chemical Physics* **2000**, *113* (22), 9901–9904. https://doi.org/10.1063/1.1329672.

(16) Henkelman, G.; Jónsson, H. Improved Tangent Estimate in the Nudged Elastic Band Method for Finding Minimum Energy Paths and Saddle Points. *The Journal of Chemical Physics* **2000**, *113* (22), 9978–9985. https://doi.org/10.1063/1.1323224.

(17) Sheppard, D.; Xiao, P.; Chemelewski, W.; Johnson, D. D.; Henkelman, G. A Generalized Solid-State Nudged Elastic Band Method. *The Journal of Chemical Physics* **2012**, *136* (7), 074103. https://doi.org/10.1063/1.3684549.

(18) Liu, C. M.; Ge, N. N.; Cheng, Y.; Ji, G. F. Structural and Elastic Properties of $LaTiO_3$ under Pressure. *Physica B: Condensed Matter* **2011**, *406* (10), 1926–1931. https://doi.org/10.1016/J.PHYSB.2011.02.055.

(19) Nye, J. F.; Lindsay, R. B. Physical Properties of Crystals: Their Representation by Tensors and Matrices. *Physics Today* **1957**, *10* (12), 26–26. https://doi.org/10.1063/1.3060200.

(20) Mouhat, F.; Coudert, F. X. Necessary and Sufficient Elastic Stability Conditions in Various Crystal Systems. *Physical Review B - Condensed Matter and Materials Physics* **2014**, *90* (22), 4–7. https://doi.org/10.1103/PhysRevB.90.224104.

(21) Chung, D. H.; Buessem, W. R. The Voigt-Reuss-Hill Approximation and Elastic Moduli of Polycrystalline MgO, CaF_2, β-ZnS, ZnSe, and CdTe. *Journal of Applied Physics* **1967**, *38* (6), 2535–2540. https://doi.org/10.1063/1.1709944.

(22) Xiao, B.; Feng, J.; Zhou, C. T.; Jiang, Y. H.; Zhou, R. Mechanical Properties and Chemical Bonding Characteristics of Cr_7C_3 Type Multicomponent Carbides. *Journal of Applied Physics* **2011**, *109* (2). https://doi.org/10.1063/1.3532038/141071.

(23) Sradhasagar, S.; Pati, S.; Roy, A. Computational Design of an Affordable, Lightweight Solid Electrolyte for All-Solid-State Lithium-Ion Batteries. *The Journal of Physical Chemistry C* **2024**. https://doi.org/10.1021/acs.jpcc.4c03260.

(24) Wan, Z.; Chen, X.; Zhou, Z.; Zhong, X.; Luo, X.; Xu, D. Atom Substitution of the Solid-State Electrolyte $Li_{10}GeP_2S_{12}$ for Stabilized All-Solid-State Lithium Metal Batteries. *Journal of Energy Chemistry* **2024**, *88*, 28–38. https://doi.org/10.1016/j.jechem.2023.09.001.

(25) Monroe, C.; Newman, J. The Impact of Elastic Deformation on Deposition Kinetics at Lithium/Polymer Interfaces. *J. Electrochem. Soc.* **2005**, *152* (2), A396. https://doi.org/10.1149/1.1850854.

(26) Nagy, K. S.; Siegel, D. J. Anisotropic Elastic Properties of Battery Anodes. *Journal of The Electrochemical Society* **2020**, *167* (11), 110550. https://doi.org/10.1149/1945-7111/aba54c.

(27) Chen, H.; Hong, T. First-Principles Investigation of the Mechanical and Thermodynamic Properties of the Metal-Borohydrides as Electrolytes for Solid-State Batteries. *Journal of The Electrochemical Society* **2019**, *166* (4), A493–A500. https://doi.org/10.1149/2.0071904JES/XML.